



## Preparation of metal-organic framework from *in situ* self-sacrificial stainless-steel matrix for efficient water oxidation

Li Zhong<sup>a</sup>, Lixiang He<sup>a</sup>, Ni Wang<sup>a,c,\*</sup>, Yunjian Chen<sup>a</sup>, Xingchen Xie<sup>a</sup>, Baolong Sun<sup>a</sup>, Jinjie Qian<sup>b,\*\*</sup>, Sridhar Komarneni<sup>c,\*\*</sup>, Wencheng Hu<sup>a</sup>

<sup>a</sup> School of Materials and Energy, University of Electronic Science & Technology of China, Chengdu 611731, PR China

<sup>b</sup> College of Chemistry and Materials Engineering, Wenzhou University, Wenzhou 325000, PR China

<sup>c</sup> Materials Research Institute and Department of Ecosystem Science and Management, 204 Energy and the Environment Laboratory, The Pennsylvania State University, University Park, PA 16802, USA



### ARTICLE INFO

#### Keywords:

Metal-organic framework  
MOF/substrate  
*In situ* growth  
Oxygen evolution  
Phase transition  
Recycle and re-use

### ABSTRACT

The oxygen evolution reaction (OER) on the anode is one of the key half-cell reactions in water electrolysis and metal-air batteries, and its reaction process is mainly hampered by sluggish kinetics and low efficiency. In this work, a series of MIL-53 metal-organic framework (MOF) derived materials grown on self-sacrificial SSM substrate was designed and synthesized for efficient water oxidation in alkaline solutions. The as-obtained FeNiBDC/SSM (SSM = stainless steel matrix and H<sub>2</sub>BDC = benzene-1,4-dicarboxylic acid) with MIL-53 MOF of uniform morphology and high porosity was successfully synthesized via a facile one-step method using recycled stainless steel as a template. Afterward, FeNiBDC/SSM was accompanied by morphological and structural changes during the OER process while the modified MOF components on the SSM substrate degraded into Fe/NiOOH species, which serve as catalytic centers. After the stability test for 100 h, the used optimal FeNiBDC/SSM2 exhibited a promising electrocatalytic OER performance with a low Tafel slope of 74.5 mV dec<sup>-1</sup>, a small overpotential of 239 mV at 10 mA cm<sup>-2</sup>, and high current retention of 95.20 %. This work provides a new research idea for the sustainable recycling of existing resources and the one-step *in-situ* preparation of MOF/substrate electrocatalyst for OER.

### 1. Introduction

Energy and environmental issues have become major concerns the world over at present, and the scientific community has paid great attention to energy storage and conversion technologies. Among numerous sustainable avenues, water-splitting has great potential in electrochemical energy conversion due to its sustainability and the use of environmentally friendly raw materials [1]. In the past years, proton exchange membrane (PEM) water electrolyzers were proposed to play a crucial role in water electrolysis due to their fast load change and energy efficiency [2,3]. In theory, the typical overall water-splitting encompasses two types of basic half-reactions, the oxygen evolution reaction (OER) and the hydrogen evolution reaction (HER). The OER process is a predominant half-reaction, which is hindered by the sluggish reaction kinetics of the stepwise 4-electron pathway as well as the low efficiency [4]. The noble metal-based electrocatalysts such as IrO<sub>2</sub> and RuO<sub>2</sub> are

considered to be excellent catalysts, which are of low abundance and high-cost [5]. PEM-based technology has matured after decades of development, and precious noble-metal-modified catalysts are shown to be competitive [6,7].

So far, research efforts have been divided into three main categories: increased intrinsic activity of catalysts through material design strategy, optimized cell/electrolyte configurations, and controlled electrode morphologies [8]. In this case, researchers have also tried to explore more economical and earth-abundant-stocks of transition metal (TM) compounds, such as Fe-, Co-, and Ni-based OER catalysts as alternatives to compensate for the constraint of scarce noble metal resources [9]. Among numerous metal compounds, type 304 stainless steel is composed of iron (~70 wt%), chromium (~15 wt%), nickel (~12 wt%), and other metals (~3 wt%), which can be used as an ideal source and substrate of TMs (Table S1)[10]. Currently, stainless steel and its derived materials have been used in the application of energy storage and

\* Corresponding author at: School of Materials and Energy, University of Electronic Science & Technology of China, Chengdu 611731, PR China.

\*\* Corresponding authors.

E-mail addresses: [niwang@uestc.edu.cn](mailto:niwang@uestc.edu.cn) (N. Wang), [jinjieqian@wzu.edu.cn](mailto:jinjieqian@wzu.edu.cn) (J. Qian), [sxk7@psu.edu](mailto:sxk7@psu.edu) (S. Komarneni).

conversion, such as urea electrolysis [11], supercapacitors, and water oxidation catalysts [12].

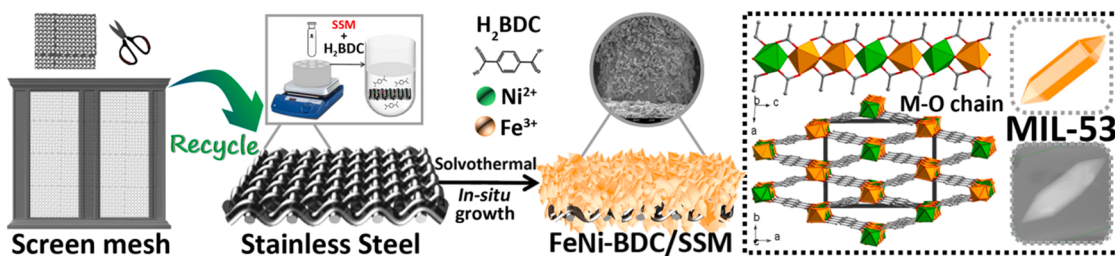
Metal-organic frameworks (MOFs) can be self-assembled by metal nodes and organic linkers, which have been applied in gas separation [13], drug delivery [14], sensor [15], fuel cells [16], water splitting [17], and metal-air batteries [18]. Among them, TM-based MOF materials have attracted great attention as competitive OER electrocatalysts due to their advantages such as controllable morphology, diverse and tunable pore environment, higher inherent porosity, and versatile structures and functions [19,20]. However, most electrocatalysts were prepared in powder form, which require the use of binders to support them on a substrate (current collector) to obtain working electrodes but the use of binders reduces the number of active sites and decreases the overall conductivity of the electrode [21,22]. Therefore, it is important to develop innovative one-step fabrication of MOF/substrate materials with strong and intimate contact, which can serve as efficient electrocatalysts.

In this work, the recovered waste stainless-steel matrix (SSM) was selected as the substrate of metal source and substrate to coordinate with benzene-1,4-dicarboxylic acid ( $H_2BDC$ ) followed by its use for in situ growth of a MOF/substrate material under simple and continuous solvothermal conditions. The composites were named FeNiBDC/SSM1/2/3/4 according to different reaction times of 4 h (FeNiBDC/SSM1), 12 h FeNiBDC/SSM2, 20 h FeNiBDC/SSM3, and 28 h FeNiBDC/SSM4 and used to determine the possible growth mechanism. The crystal structure of FeNiBDC/SSM is ascribed to the MIL-53(Fe/Al/Cr) (Material of Institute Lavoisier), which consists of one-dimensional (1D) chains of trans  $\mu$ -OH corner sharing MO<sub>6</sub>-octahedra [23] (Scheme 1). Hence, the as-prepared FeNiBDC/SSM is expected to act as an anode of OER half-reaction to assemble an electrolytic water device with a HER electrode and alkaline electrolyte membrane (AEM) to achieve efficient water electrolysis in alkaline solution. The performance can be assigned to merits of FeNiBDC/SSM with uniform bipyramidal hexagonal prism morphology, large surface area, high porosity, good crystalline form, and bimetal synergistic effect, along with the low resistance and robust structure of SSM substrate, and abundant metal source as self-sacrificial template.

## 2. Experiment

### 2.1. Chemicals

All chemicals and solvents can be used directly without further purification. Terephthalic acid ( $H_2BDC$ , 99 %, Chengdu Kelong Reagent of China), hydrochloric acid (HCl, 99 %, 6.0 M, Chengdu Kelong Reagent of China), sodium hydroxide (NaOH, 99.0 %, Chengdu Kelong Reagent of China), sodium silicate (Na<sub>2</sub>SiO<sub>3</sub>, 99.9 %, Chengdu Kelong Reagent of China), sodium dodecyl sulfate (SDS, 99 %, Chengdu Kelong Reagent of China) and polyoxyethylene octylphenol ether (99.0 %, Chengdu Kelong Reagent of China), the standard sample ruthenium dioxide (RuO<sub>2</sub>, 99.9 %, Chengdu Kelong Reagent of China), and *N*, *N*-Dimethylformamide (DMF, ≥99.5 %, Chengdu Kelong Reagent of China), ethanol (95 %, EtOH, Chengdu Kelong Reagent of China), and ultra-pure water (DI).



**Scheme 1.** Schematic synthesis of FeNiBDC/SSM composite. The FeNiBDC/SSM was in situ grown on the waste stainless steel under solvothermal conditions. The dotted box is the crystal structure of MIL-53, it has long chains of M-O connection.

### 2.2. Recycled waste SSM

The optimal recycled treatment detail is as follows. First, cut  $1 \times 1$  decimetre stainless steel mesh from the discarded stainless steel screen mesh. Then this SSM mesh was added into a configured degreasing solution containing NaOH (15 g L<sup>-1</sup>), Na<sub>2</sub>SiO<sub>3</sub> (10 g L<sup>-1</sup>), sodium dodecyl sulfate (0.25 g L<sup>-1</sup>), and polyoxyethylene octylphenol ether (0.25 g L<sup>-1</sup>), which is heated to 60 °C for 4 h (unless otherwise mentioned, SSM only refers to the optimal condition of recycled treatment for 4 h). The comparison of the effect of different degreasing times (0, 1, and 4 h) on recycled stainless steel was explored as depicted in Fig. S1.

### 2.3. Synthesis of FeNiBDC/SSM1

After drying and cleaning, these recycled SSM was immersed in an HCl solution (6.0 M) to remove the oxidation layer. After that,  $H_2BDC$  (organic linker, 600 mg) and cleaned SSM (metal sources,  $2 \times 2$  cm<sup>2</sup>) were put into a pressure-resistant tube, and 12 mL of DMF, 2 mL of water, and 3 mL of configured HCl were added. These solutions were stirred and heated for 4 h (1200 rpm), then the material (denoted as FeNiBDC/SSM1) was easily collected by washing and drying at 80 °C overnight. By changing the heating hours to 12, 20, and 28, samples designated as FeNiBDC/SSM2, FeNiBDC/SSM3, and FeNiBDC/SSM4 were also prepared respectively.

## 3. Results and discussion

### 3.1. Characterization of FeNiBDC/SSM

The crystal type of FeNiBDC/SSM1/2/3/4 can be assigned to the typical and flexible MIL-53 structure, in which the oxygen atoms are coordinated to the Fe<sup>3+</sup> and Cr<sup>3+</sup> metals ions by assembling corner-sharing MO<sub>6</sub> octahedra. The asymmetric unit of MIL-53 contains three types of metal atoms, the Fe atoms can be partially replaced by Ni or Cr atoms (Fig. S2) [24]. Fig. 1a shows a flexible 1D channel of MIL-53 composed of intersecting corner-sharing octahedrons, and the metal nodes of the FeO<sub>6</sub> octahedron can be partially replaced by NiO<sub>6</sub>, thus bringing about a new structure (chromium coordination is mostly neglected due to the low Cr: Fe ratio in the stainless-steel content and the low dissolved Cr content during the experiment). Scanning electron microscopy (SEM) was used to check the morphological evolution of FeNiBDC/SSM with different reaction times, which roughly passed through the same process as shown in Fig. 1b and Fig. S3. After the reaction for 4 h, the SEM image of FeNiBDC/SSM1 (Fig. S2a) shows that the smooth surface of the blank SSM substrate was etched and a layer of crystals formed gradually. After the reaction for 12 h, FeNiBDC/SSM2 (Fig. S3b) exhibited a bipyramidal hexagonal prism morphology, while the size, uniformity, and coverage on the SSM surface increased slightly. With the further prolongation of the reaction time as in the case of FeNiBDC/SSM3 (Fig. S3c), the coverage of crystals increased further. The increased coverage with crystals was accompanied by the grain cracking on the surface as a result of the structural stress. Meanwhile, rapid nucleation was followed by slow growth, resulting in particles of

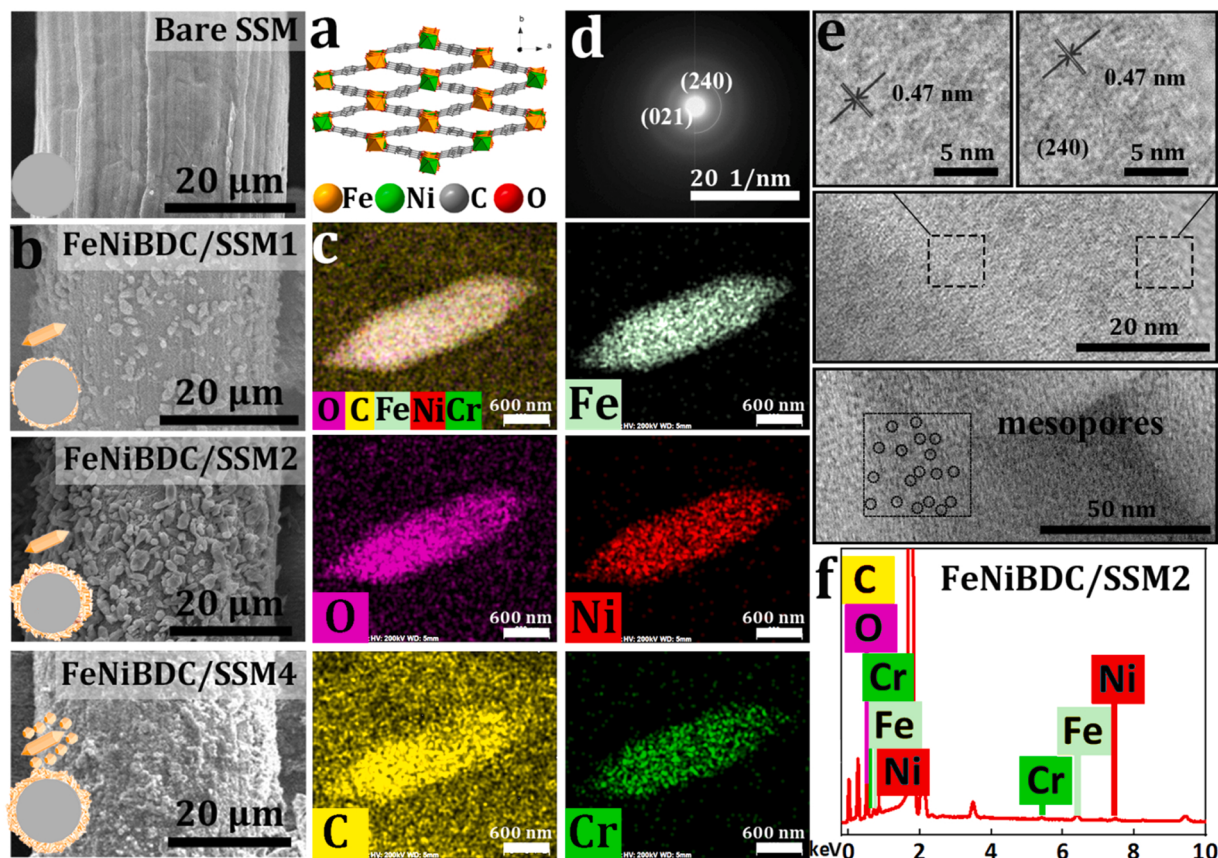


**Fig. 1.** (a) The unit cell of MIL-53, (b) SEM images of bare SSM and FeNiBDC/SSM1/2/4, respectively. (c) the elemental mapping images of FeNiBDC/SSM2. (d) SAED patterns, (e) HRTEM and lattice fringes, and (f) EDS spectra of FeNiBDC/SSM2, respectively.

FeNiBDC/SSM4 with smaller sizes (Fig. S3d). Due to the similarity between FeNiBDC/SSM2 and FeNiBDC/SSM3, only FeNiBDC/SSM2 sample was selected for comparison. Furthermore, transmission electron microscopy (TEM) images of the morphology changes during the synthesis are shown in Fig. S4. Herein, FeNiBDC/SSM2 was selected for detailed characterization and testing due to the structural integrity and economics of shorter reaction times. In Fig. 1c, the as-obtained FeNiBDC/SSM2 exhibits a clear bipyramidal hexagonal prism morphology with uniform distribution of C, O, Cr, Fe, and Ni elements. Selected area electron diffraction (SAED) of the clear area on the surface shows diffuse rings, which suggest a weakly crystalline nature due to the destruction of the crystal form caused by the dissolution and competitive coordination of poly-metals (Fig. 1d). The diffraction rings correspond to the (240) and (021) planes of MIL-53 structure, respectively. The high-resolution TEM (HR-TEM) in Fig. 1e suggests the main lattice fringes of 0.47 nm could be attributed to the (240) / (021) plane of MIL-53 [25]. It is worth noting the existence of numerous mesopores as can also be observed (scale bar is 50 nm), which is favorable for accelerating electron transfer during the OER process. Similar to the mapping, the energy dispersive spectra (EDS) in Fig. 1f prove the distribution of C, O, Fe, Ni, and Cr elements. Furthermore, the thermogravimetric analysis also confirms the structural information as depicted in Fig. S5.

A schematic diagram for in situ growth of FeNiBDC/SSM is shown in Fig. 2a. In the beginning, pure SSM, ligand ( $H_2BDC$ ), solvent (DMF and DI), and hydrochloric acid solution (etchant), were added to the pressure tube, and the solution is colorless and transparent (Step I). Heating overcomes the reaction's energy barrier and brings on slow accumulation via hydrolysis reaction of DMF catalyzed by the protons generated during deprotonation of ligand (terephthalic acid). In detail, the corrosion process took place when the hydrochloric acid molecules attacked the stainless steel. The reaction of deprotonated carboxyl groups with

dissolving metal ions simultaneously occurred resulting in the clear solution of light green color (Step II). After continuous heating, these metal ions coordinate with the oxygen on the ligand to form the  $FeO_6$  cluster partially replaced by Ni or Cr atoms, which were determined by the competitiveness of metal ions including metal content, ionic hydrated radius, dissolution rate, and coordination rate [26,27]. In this process, the formate species partially incorporates nuclei and crystals, possibly serving as regulators for the morphology and/or creating defects in the structure. After that, the agglomeration of nuclei takes place, accompanied by the release of monomeric species to the solution, hence confirming that solid-solid crystallization is in action (Step III) [28]. The continuous etching of the SSM surface and the dissolution of ions provide a sufficient metal source for subsequent coordination growth. As the coordination progresses, the metal ions and ligands continue to coordinate to form more crystalline MOF. At this time, reddish-brown dense MIL-53(Fe, Ni, Cr) crystals are precipitated on the SSM, and the pressure tube is uniformly light brown (Step IV). Subsequently, the structure and phase transition of FeNiBDC/SSM were studied by powder X-ray diffraction patterns (PXRD) and Raman spectra (532 nm). The substrates and the corresponding powder have been chosen to better compare and illustrate the growth trend. The FeNiBDC/SSM1 was partially grown on the SSM substrate, and the background signal exhibits a broad peak around  $13.6^\circ$  due to the strong intensity of the substrate's basal peaks (Fig. 2b). With the prolongation of the reaction time, these dissolved ions including Fe, Ni, and Cr cations with similar radius and coordination number continuously coordinate with the ligand, tending to perfect the crystal structure. In the XRD spectrum of FeNiBDC/SSM2, there are several clear peaks at  $18.18^\circ$  and  $18.46^\circ$ , which correspond to the (320) and (400) planes of the typical MIL-53 structure. In addition, the peaks of FeNiBDC/SSM2 at  $21\text{--}23^\circ$  are assigned to impurity, resulting from competitive coordination between

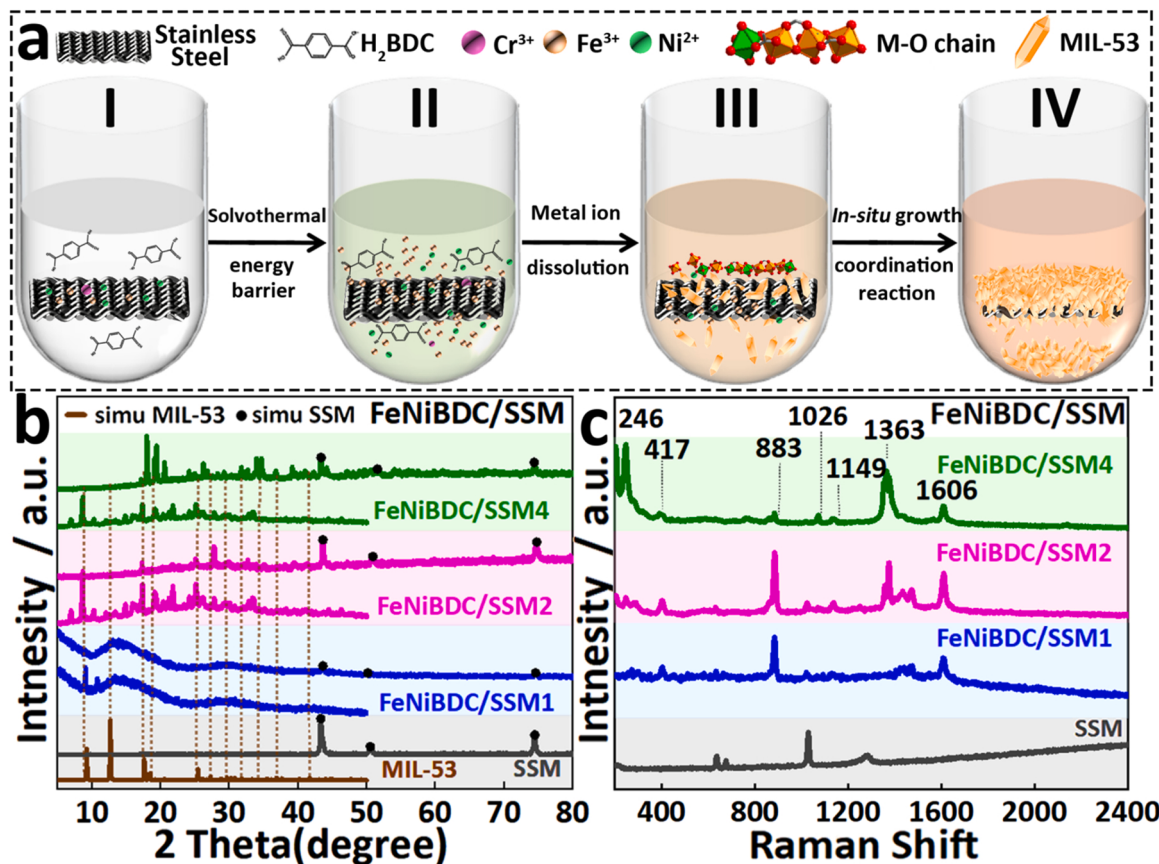


**Fig. 2.** (a) Schematic diagram for the growth of FeNiBDC/SSM composite (Step I-IV). A waste stainless steel was selected as the metal source, and the MOF material was grown in situ under solvothermal conditions. (b) PXRD patterns, and (c) Raman spectra of FeNiBDC/SSM.

three different metal cations ( $\text{Fe}^{3+}$ ,  $\text{Ni}^{2+}$ , and  $\text{Cr}^{3+}$ ) during the coordination process. After a reaction time of 28 h, MIL-53 is still the main phase of FeNiBDC/SSM4, while the presence of multiple peaks and peak shifting in FeNiBDC/SSM4 is attributed to multimetallic coordination and destruction of MOF's structure. Competitive coordination of another crystal structure (such as MIL-88) also leads to the appearance of multiple peaks [29], which is related to the similar ligand, reaction temperature, and solvents. In addition, the detailed trend of these series is depicted in Fig. S6. The surface chemical bonding of the FeNiBDC/SSM structure has also been measured by Raman spectroscopy as shown in Fig. 2c. However, the Raman signal of the SSM is very weak, probably due to the strong response of alloy species [30]. As the coordination progresses, the Raman spectra suggest that the peaks of FeNiBDC/SSM1 are located at 417, 883, and  $\sim 1363 \text{ cm}^{-1}$ . Subsequently, the signal of

FeNiBDC/SSM2 at  $246 \text{ cm}^{-1}$  is obvious, which could be ascribed to the MOF coordination. After that, the MOF signal of FeNiBDC/SSM4 can be clearly observed, which further proves the successful synthesis of MOF on the substrate.

Adsorption isotherm is an indispensable tool for studying the pore structure of different materials, which contains abundant structural information. Therefore, the specific surface area (SSA) and pore size distribution of these MOF composites (0.6 square centimeters) were further analyzed by nitrogen adsorption. In Fig. 3a-3c, the adsorption capacity values of FeNiBDC/SSM1/2/4 are 54.2, 91.7, and  $84.8 \text{ cm}^3 \text{ g}^{-1}$ , respectively. The specific surface areas of FeNiBDC/SSM1/2/4 are 21.49, 25.63, and  $23.47 \text{ m}^2 \text{ g}^{-1}$ , respectively, which were calculated from nitrogen adsorption isotherms using the Brunauer-Emmett-Teller (BET) model. In comparison, the extremely low adsorption capacity

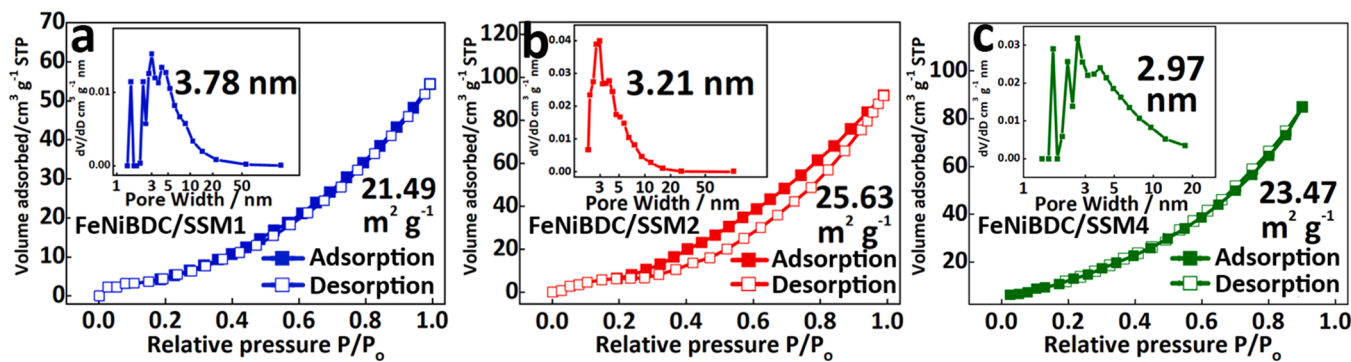


**Fig. 3.** N<sub>2</sub> isotherms (closed, adsorption; open, desorption) for (a) FeNiBDC/SSM1, (b) FeNiBDC/SSM2, and (c) FeNiBDC/SSM4, respectively. Insets are their corresponding pore size distributions (PSD).

value of blank SSM leads to only a  $1.43 \text{ m}^2 \text{ g}^{-1}$ , which proves that FeNiBDC/SSM structure with high adsorption capacity and porosity was successfully prepared by the modification strategy of SSM substrate (Fig. S7). Notably, the adsorption capacity of FeNiBDC/SSM is not particularly good compared to the theoretical MIL-53 powder, which may be attributed to the much lower actual loaded MOF content of SSM compared to that of pure MIL-53 powder. At the same time, the modification may be accompanied by incomplete morphological development and the formation of defects during crystallization, which also leads to a decrease in adsorption capacity and specific surface area [31]. The PSD curves of FeNiBDC/SSM suggest that a large number of mesopores exist, with a maximum pore size of 3.78, 3.21, and 2.97 nm, respectively. In this case, the hierarchical porosity of FeNiBDC/SSM may expose more active sites with large pore volumes, which contributes to faster ion and electrolyte transport.

Furthermore, X-ray photoelectron spectroscopy (XPS) is a surface chemical analysis technique that can determine the composition, experimental formula and chemical state of elements of the target materials. Therefore, XPS was used to analyze the valence information due to its testing simplicity, non-structural destructiveness, and sensitivity. The high-resolution spectra of C 1 s, Fe 2p, and Cr 2p in FeNiBDC/SSM1, FeNiBDC/SSM2, and FeNiBDC/SSM4 exhibit slight differences. As shown in Fig. 4a, the survey spectrum indicates the presence of Ni, Fe, Cr, O, and C elements. Specifically, the C 1 s signals of FeNiBDC/SSM2 in Fig. 4b are attributed to the ligand of MIL-53 structure, which can be deconvoluted into three peaks at 288.3 eV ( $\text{C}=\text{O}$ ), 286.2 eV ( $\text{C}-\text{O}$ ), and 285.0 eV ( $\text{C sp}^2$ ), respectively. In Fig. 4c, the signals of Fe 2p<sub>1/2</sub> (725.5 eV) and Fe 2p<sub>3/2</sub> (711.9 eV) are deconvoluted into three

components,  $\text{Fe}^{3+}$  (725.6 and 712.0 eV),  $\text{Fe}^{2+}$  (723.1 and 709.4 eV), and satellites peaks [32]. Meanwhile, in Fig. 4d, two sets of sub-peaks in the deconvoluted Ni 2p pattern at 874.3 and 856.3 eV are attributed to Ni 2p<sub>1/2</sub> and Ni 2p<sub>3/2</sub>. Specifically, the binding energy of  $\text{Ni}^{3+}$  (875.5 and 857.9 eV) and  $\text{Ni}^{2+}$  (873.7 and 856.3 eV), suggest that the main species are Ni(II). In addition, the XPS signal of Cr 2p can be assigned to  $\text{Cr}^{4+}$  (588.9 and 578.9 eV),  $\text{Cr}^{3+}$  (587.2 and 576.9 eV), and  $\text{Cr}^0$  (585.1 and 574.8 eV), respectively. The high-resolution O 1 s spectrum was fitted into two characteristic peaks of  $\text{C}-\text{O}/\text{C}=\text{O}$  (532.5 eV) and metal-O (531.6 eV) (Fig. S8) [33]. The detailed XPS data has been summarized in Tables S2 and S3.

### 3.2. Morphological and structural characterizations of FeNiBDC/SSM

After the long-term anodic reaction, the electrolyzed FeNiBDC/SSM2 is termed FeNiBDC/SSM-OER. More details of characterizations and electrochemical measurements are depicted in the SI. To explore the stability of FeNiBDC/SSM-OER, the morphological and structural changes during electrocatalysis were investigated, which is denoted as FeNiBDC/SSM-OER(I-III) at different cyclic voltammogram cycles (1, 50, and 100 cycles). In Fig. 5a, the initial samples have a uniform topography. After 1 cycle, weak surface solvation occurred at this time, and the morphology of FeNiBDC/SSM-OER(I) hardly changed. After 50 cycles, under the action of electrolyte solvation, observable partial degradation has occurred, with the morphology and size of FeNiBDC/SSM-OER(II) having changed, and some nano/micron particles have appeared on the surface due to degradation. Subsequently, abundant nanosheets with a larger size emerged on the modified substrate after

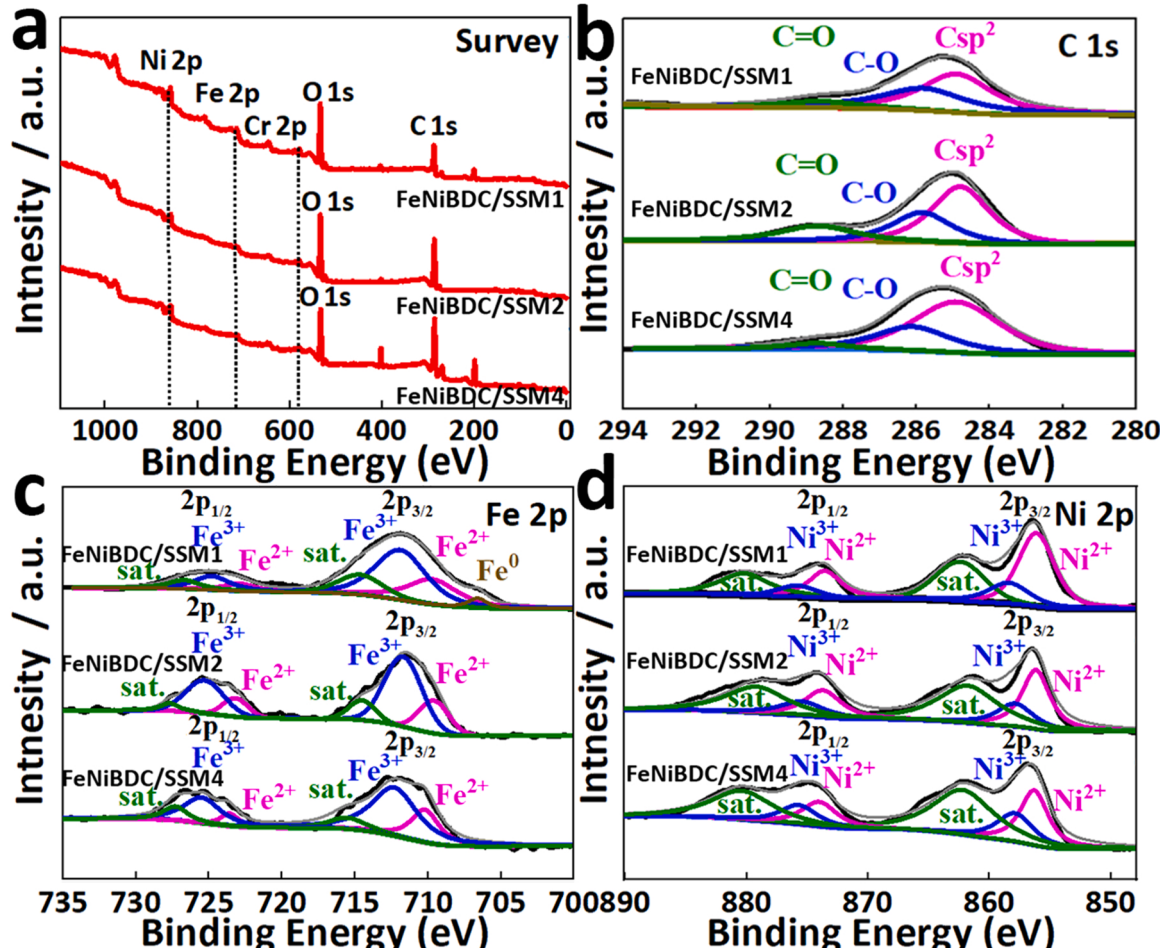
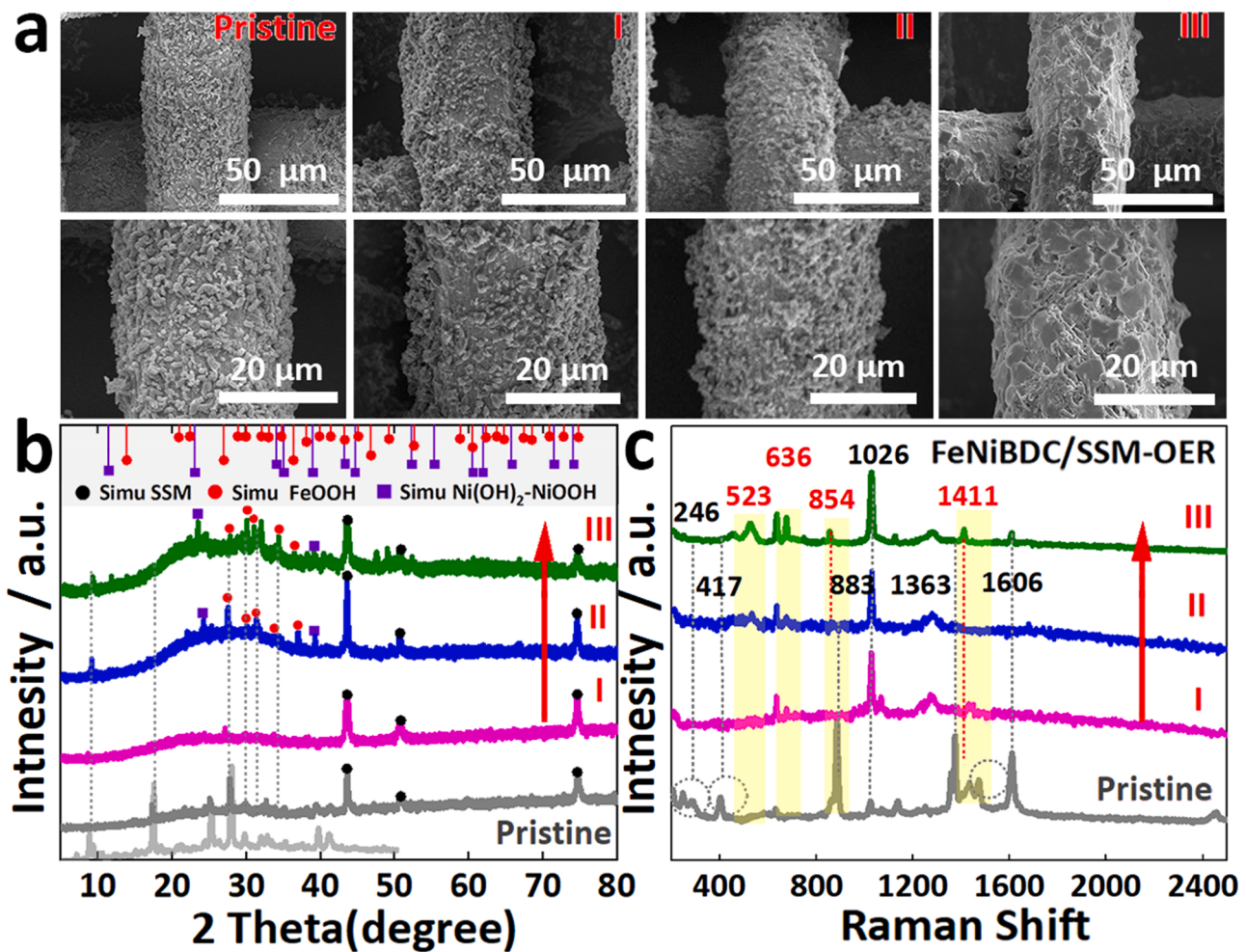


Fig. 4. XPS comparison between FeNiBDC/SSM1, FeNiBDC/SSM2, and FeNiBDC/SSM4 for the (a) full survey, (b) C 1 s, (c) Fe 2p, and (d) Ni 2p, respectively.



**Fig. 5.** (a) SEM images of four states of degradation from the initial catalyst FeNiBDC/SSM2 to FeNiBDC/SSM-OER(I-III). (b) XRD patterns, and (c) Raman spectra of FeNiBDC/SSM-OER(I-III) (after 1, 50, and 100 cycles), respectively.

100 cycles, along with the shedding of MOF crystals while the rough surface of the modified SSM can still be observed. The changes that occurred during the OER process were characterized by XRD (Fig. 5b), which shows that the original peak of FeNiBDC/SSM2 is weak but several new peaks could be observed. After prolonged cycling, peaks were observed at 21.9° and 39.3°, which are attributed to Ni(OH)<sub>2</sub>-NiOOH (JCPDS No. 06-0044) while additional peaks at 27.5°, 30.0°, 32.1°, 33.6°, and 36.5° may have resulted from the main species of FeOOH (JCPDS No. 01-0136) [34]. The corresponding Raman spectra provide more evidence for structural evolution. As shown in Fig. 5c, the signal of FeNiBDC/SSM2 at 246 and 417 cm<sup>-1</sup> has nearly disappeared after cycling, the signals at 1363 and 1606 cm<sup>-1</sup> were significantly weakened, while the peaks at 523, 636, 854, and 1411 cm<sup>-1</sup> were enhanced (MOH<sub>x</sub> signal) [35–37]. The MIL-53 is the template for the active species of Fe/NiOOH while SSM is serving as the modified substrate which contributes to the subsequent long-term electrocatalytic performance. In addition, the adsorption isotherm suggests that FeNiBDC/SSM-OER exhibits a large specific surface area and an abundant porosity even after cycling, apparently providing more space for electron transfer (Fig. S9).

In order to get more information about the changes in the materials after the electrocatalytic process, XPS measurement was carried out to characterize FeNiBDC/SSM2 and FeNiBDC/SSM-OER before and after the OER process. The full survey spectrum shows that Ni, Fe, Cr, O, and C elements still existed after the OER cycle, while the element intensities of FeNiBDC/SSM-OER are differentially attenuated (Fig. 6a). This

reduction is especially pronounced for Cr as indicated by Cr signal, which suggests lower content of Cr due to its dissolution during the process. In Fig. 6b, three different signals, including satellite peak (288.0 eV), C=O (285.8 eV), and C sp<sup>2</sup> (284.7 eV) are found in the C 1 s XPS spectrum of FeNiBDC/SSM-OER, revealing the decomposition and dissolution of MOF framework [38,39]. Meanwhile, the C=O (288.3 eV) signal disappears and other signals shift to low binding energy after OER cycling. To estimate and verify the phase transformation, the O 1 s XPS peaks of FeNiBDC/SSM-OER were studied, as shown in Fig. 6c. Compared to C=O and M-O species of FeNiBDC/SSM, M-OH (532.1 eV) and M-O (530.8 eV) signals appeared after cycling, which can be attributed to the Fe/NiOOH component of FeNiBDC/SSM-OER. Two types of Fe 2p peaks of FeNiBDC/SSM-OER including Fe 2p<sub>1/2</sub> (725.2 eV) and Fe 2p<sub>3/2</sub> (712.1 eV) show a decreasing trend (Fig. 6d), which confirms the decomposition of FeNiBDC/SSM2 after electrocatalysis. In Fig. 6e, the Ni 2p signal of composition before (874.3 and 856.3 eV) and after the cycle (874.0 and 856.1 eV) can be used for comparison, which suggests a shift to higher binding energy after electrocatalysis. Meanwhile, a transition in the valence state from Ni(II) to Ni(III) can be observed, which is correlated to the generation of NiOOH species during the electrochemical process. The Fe/NiOOH species of FeNiBDC/SSM2 have more active surface area and lower electron transfer resistance, which is consequently beneficial to promoting the OER process. During the catalytic process, the Cr ions dissolved into the electrolyte, resulting in an obvious drop in the Cr 2p signal [40] (Fig. 6f). All the data of the XPS spectra of the FeNiBDC/SSM2/-OER series are

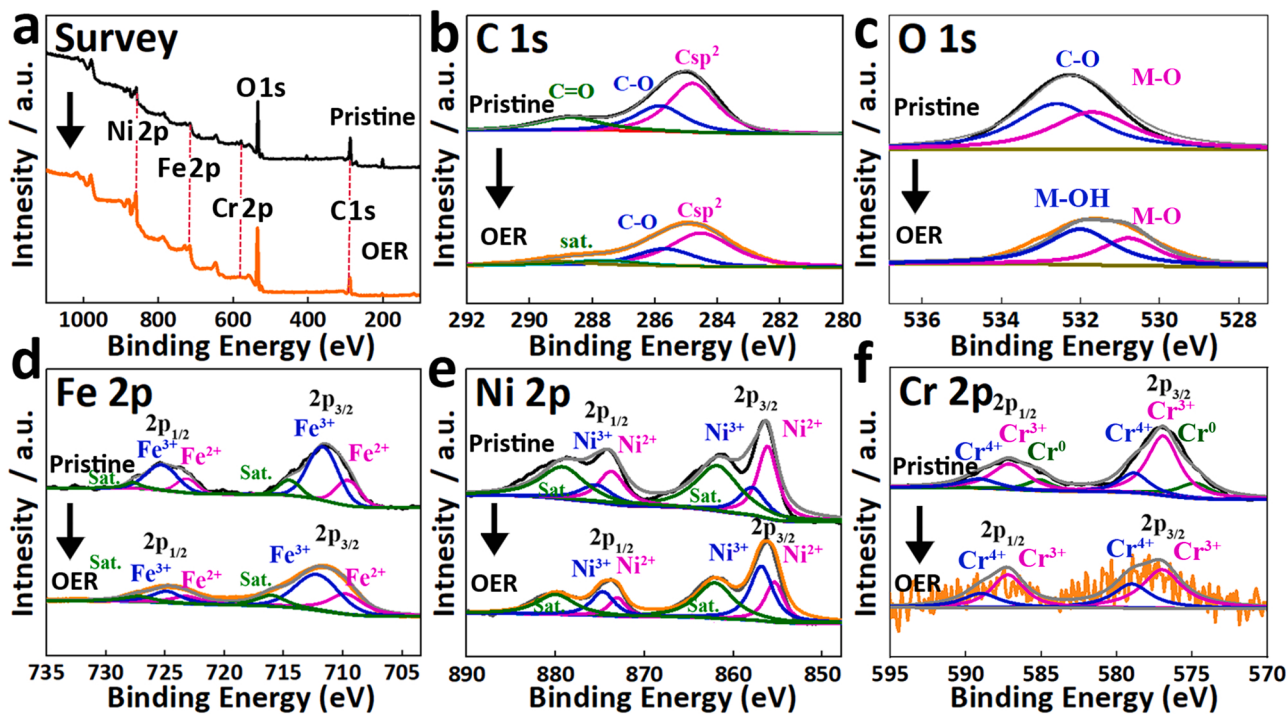


**Fig. 6.** XPS comparison between FeNiBDC/SSM2 and FeNiBDC/SSM-OER for the (a) full survey spectrum, (b) C 1 s, (c) O 1 s, (d) Fe 2p, (e) Ni 2p, and (f) Cr 2p, respectively.

summarized in Table S4.

### 3.3. Electrochemical activity of FeNiBDC/SSM1/2/3/4

In Fig. 7a, the overpotential values at  $10 \text{ mA cm}^{-2}$  ( $\eta_{10}$ ) of FeNiBDC/SSM1/2/3/4 and commercial RuO<sub>2</sub> catalyst are found to be 344, 239, 311, 290, and 262 mV at  $10 \text{ mA cm}^{-2}$ , respectively. In this case, the obtained FeNiBDC/SSM2 exhibits the best OER activity, reaching the highest current density of  $119.0 \text{ mA cm}^{-2}$  at 1.7 V (all applied potentials were calibrated with a reversible hydrogen electrode (RHE)). At 1.7 V, FeNiBDC/SSM1/3/4 and commercial RuO<sub>2</sub> catalyst attained 60.4, 81.1, 51.3, and  $121.3 \text{ mA cm}^{-2}$ , respectively. The cyclic voltammogram (CV) curves of FeNiBDC/SSM exhibits a similar oxidation peak, which comes from the conversion of  $\text{Ni}^{2+}$  to  $\text{Ni}^{3+}$  (Fig. S10) [41]. The Tafel slopes, an essential experimental parameter to determine and assess OER kinetics, were calculated to be 91.8, 74.5, 96.8, 121.2, and  $89.72 \text{ mV dec}^{-1}$  for FeNiBDC/SSM1/2/3/4 and commercial RuO<sub>2</sub> samples, respectively (Fig. 7b). For comparison, commercial and recycled SSM templates were used to synthesize FeNiBDC/SSM2 (Fig. S11), which showed virtually no difference in the preparation of FeNiBDC/SSM2, proving the effectiveness of our recycling strategy. Meanwhile, other materials such as pure nickel foam, pure SSM, and adhesive-coated Nickel foam have been tested and compared with in-situ grown FeNiBDC/SSM2 for their performance, which suggests the superiority of the self-sacrifice and in-situ growth strategy (Fig. S12). The polarization curves at different scan rates have also been collected as shown in Fig. S13. Electrochemical impedance spectroscopy (EIS) is an important method to evaluate the interfacial charge transfer behavior, and the parameters can be analyzed by fitting them to the Nyquist curve. As shown in Fig. 7c, the charge transfer resistance ( $R_{ct}$ ) of FeNiBDC/SSM1/2/3/4 electrocatalysts are 5.7, 2.1, 7.0, and  $18.0 \Omega$ , respectively. Among them, FeNiBDC/SSM2 has the lowest interfacial resistance, indicating a faster charge transfer process. The calculated double-layer capacitance ( $C_{dl}$ ) values of FeNiBDC/SSM1/2/3/4 samples are 0.34, 1.14, 0.92, and  $0.64 \text{ mF cm}^{-2}$ , respectively (Fig. 7d, S14). The highest value of FeNiBDC/SSM2 is correlated with the maximum

active area, large specific surface area, and abundant porosity. To explore the reaction mechanism, a rotating ring-disk electrode (RRDE) with  $E_{ring} = 1.45 \text{ V}$  was used to observe the peroxide intermediate during the OER reaction. In Fig. 7e, the ring current is almost negligible compared to the disk current. The calculated average electron transfer number ( $N$ ) is 3.95, proving that it is almost a quasi-four-electron process. Similarly, the as-calculated Faraday efficiency is 96.57 % as shown in Fig. S15. In addition, the FeNiBDC/SSM2 has been selected for stability test experiments, which has shown a retention ratio of 99.95 % even after long cycling of 10 h (Fig. S16). Afterwards, long cycling of 100 h has been explored at 1.47 V, FeNiBDC/SSM2 shows weak decay but still maintains a high current retention rate of 95.20 % after cycling, while commercial RuO<sub>2</sub> catalyst exhibits a current retention rate of 88.65 % after 40 h of testing (Fig. 7f). Furthermore, after cycling for 100 h, the polarization curves suggest that the overpotential of samples only increases by 39 mV, but the maximum current density is almost unchanged (Fig. S17). Finally, the overall electrochemical performance of the FeNiBDC/SSM1/2/3/4 series is listed in Table S5. Among them, FeNiBDC/SSM2 has the best performance with  $\eta_{10}$  of 239 mV, Tafel slope of  $74.5 \text{ mV dec}^{-1}$ ,  $R_{ct}$  resistance of  $2.1 \Omega$ , and  $C_{dl}$  value of  $1.14 \text{ mF cm}^{-2}$ , which is also competitive with many previously reported SSM derived TM-based catalysts shown in Tables S6, S7. Density functional theory (DFT) calculations were previously reported by Goddard\* et al. [42,43] to analyze the electronic structures of Fe/NiOOH, which is a suitable case that could be applied in this context. The atomic models were constructed on a layer of  $\gamma\text{-FeOOH}$  (010) (Fig. 7g). Single nickel atoms were doped into the lattice of FeOOH to substitute the positions of Fe atoms, denoted as Fe(Ni)OOH. The Ni atom was in the center of six oxygen atoms, presenting an edge-sharing connection to adjacent Fe octahedra via two bridging oxygens. In Fig. 7h, the DFT results show that the O-formation is the PDS in Fe(Ni)OOH, as in NiOOH. The beneficial effect of Ni incorporation into FeOOH is stabilizing the key intermediate, O<sup>-</sup>, thereby lowering the  $\eta$  and increasing the electrocatalytic activity for OER. Specifically, it can be divided into the following states: *State I-II*: The high-spin  $d_4$   $\text{Fe}^{4+}$  site stabilizes the unpaired electrons of key O-intermediate (on the  $\text{Fe}^{4+}$  site's surface) to

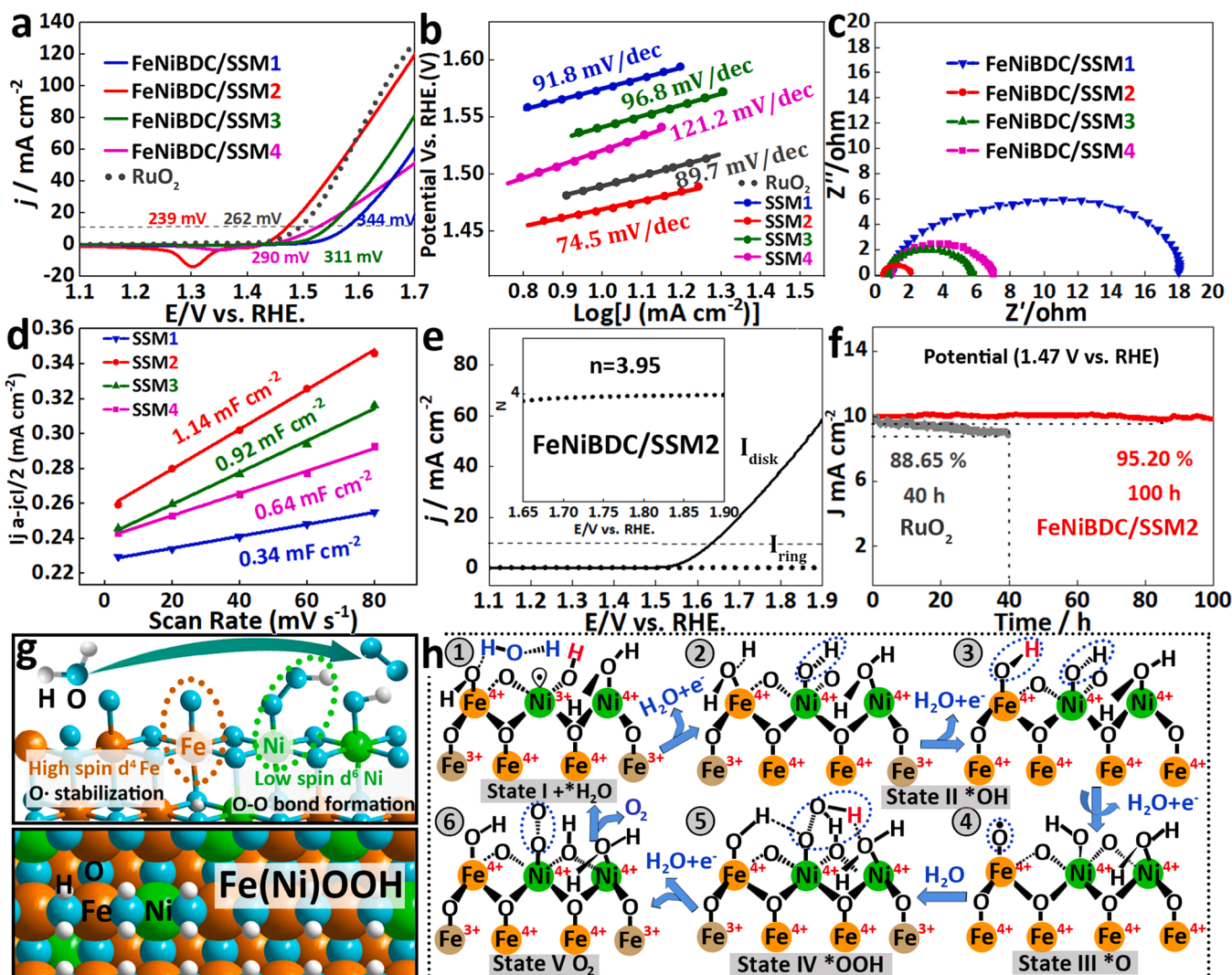


**Fig. 7.** (a) OER polarization curves and (b) Tafel plots of FeNiBDC/SSM series. (c) EIS of FeNiBDC/SSM series. (d) Liner fitting of  $C_{dl}$  values. (e) RRDE test of FeNiBDC/SSM2, and its inset shows the electron transfer number. (f) the Amperometric (I-t) diagram of FeNiBDC/SSM2 and commercial RuO<sub>2</sub>. (g) Mechanistic studies and schematic structure model of Fe(Ni)OOH from top views. (h) OER mechanism of Fe(Ni)OOH combined with previous reports [42,43].

reduce energy consumption. *State III*: O-O coupling is more likely to occur at the lower spin d<sub>6</sub> Ni<sup>4+</sup>, which is achieved by the interaction of the O<sup>-</sup> with an additional water molecule, hydrogenated the bridging oxygen between the Ni<sup>4+</sup> sites. *State IV*: The OOH formation on Ni<sup>4+</sup> results in O-O coupling, whereas O-O coupling on Fe<sup>4+</sup> is endothermic, which indicates that both Fe<sup>4+</sup> and Ni<sup>4+</sup> play an important bifunctional role in OER catalysis. *State V*: A fourth oxidation occurs, with deprotonation of the adsorbed Ni<sup>4+</sup> to form O<sup>2-</sup>. The Fe<sup>4+</sup> site facilitates the generation of the O<sup>-</sup>, while the Ni<sup>4+</sup> sites stabilize O-O coupling, thus releasing the final product of oxygen molecules. These calculations explain why Fe(Ni)OOH has better OER activity than pure Fe/NiOOH, and thus, lead to an understanding of the bifunctional nature of the catalysis with the Fe(Ni)OOH catalyst for OER with both Ni and Fe being essential for high OER activity.

#### 4. Conclusion

In conclusion, we proposed a novel one-step in situ synthesis of FeNiBDC/SSM materials on an SSM substrate, to serve as highly stable OER electrocatalysts. Among them, FeNiBDC/SSM2 exhibited the best performance with an overpotential of 239 mV, a Tafel slope of 74.5 mV dec<sup>-1</sup>, and a high current retention rate of 95.20 % after stability testing for 100 h. This may be attributed to the robust framework provided by

the modified stainless-steel substrate along with the in situ grown MOFs with uniform morphology, high porosity, good crystallinity, and multi-metal synergistic catalytic sites, all these factors were beneficial for the long-lasting water oxidation process. This work explores the relationship between phase state, morphology, crystal form, porosity, and its electrocatalytic performance, providing a new research idea for the sustainable recycling of existing resources while also proposing a one-step in situ growth method of MOF on self-sacrificial SSM substrate.

#### CRediT authorship contribution statement

**Li Zhong:** Conceptualization, Methodology, Formal analysis, Investigation, Data curation, Writing – original draft, Writing – review & editing. **Lixiang He:** Investigation, Methodology, Data curation. **Ni Wang:** Project administration, Funding acquisition, Resources, Conceptualization, Writing – review & editing. **Yunjian Chen:** Investigation, Methodology. **Xingchen Xie:** Investigation, Data curation. **Baolong Sun:** Investigation, Data curation. **Jinjie Qian:** Project administration, Resources, Conceptualization. **Sridhar Komarneni:** Resources, Supervision, Writing – review & editing. **Wencheng Hu:** Conceptualization, Writing – review & editing.

## Declaration of Competing Interest

The authors declare that they have no known competing financial interests or personal relationships that could have appeared to influence the work reported in this paper.

## Data Availability

Data will be made available on request.

## Acknowledgments

This work was financially supported by the Sichuan Science and Technology Program (No. 2021YFH0186) and the National Natural Science Foundation of China (Grant No. 51902041).

## Author contributions

The manuscript was written through the contributions of all authors. All authors have approved the final version of the manuscript.

## Appendix A. Supporting information

Supplementary data associated with this article can be found in the online version at [doi:10.1016/j.apcatb.2022.122343](https://doi.org/10.1016/j.apcatb.2022.122343).

## References

- [1] N.T. Suen, S.F. Hung, Q. Quan, N. Zhang, Y.J. Xu, H.M. Chen, Electrocatalysis for the oxygen evolution reaction: recent development and future perspectives, *Chem. Soc. Rev.* 46 (2017) 337–365.
- [2] D. Kulkarni, A. Huynh, P. Satjaritanun, M. O'Brien, S. Shimpalee, D. Parkinson, P. Shevchenko, F. DeCarlo, N. Danilovic, K.E. Ayers, C. Capuano, I.V. Zenyuk, Elucidating effects of catalyst loadings and porous transport layer morphologies on operation of proton exchange membrane water electrolyzers, *Appl. Catal. B.* 308 (2022), 121213.
- [3] M. Bernt, A. Hartig-Weiß, M.F. Tovini, H.A. El-Sayed, C. Schramm, J. Schröter, C. Gebauer, H.A. Gasteiger, Current challenges in catalyst development for PEM water electrolyzers, *Chem. Ing. Tech.* 92 (2020) 31–39.
- [4] Z.P. Wu, X.F. Lu, S.Q. Zang, X.W. Lou, Non-noble-metal-based electrocatalysts toward the oxygen evolution reaction, *Adv. Energy Mater.* 30 (2020) 1910274.
- [5] T. Weber, J. Pfrommer, M.J.S. Abb, B. Herd, O. Khalid, M. Rohnke, P.H. Läkner, J. Evertsson, S. Volkov, F. Bertram, R. Znaiguiua, F. Carla, V. Vonk, E. Lundgren, A. Stierle, H. Over, Potential-induced pitting corrosion of an IrO<sub>2</sub>(110)-RuO<sub>2</sub>(110)/Ru(0001) model electrode under oxygen evolution reaction conditions, *ACS Catalysis* 9 (2019) 6530–6539.
- [6] C.V. Pham, M. Bühler, J. Knöppel, M. Bierling, D. Seeger, D. Escalera-López, K.J.J. Mayrhofer, S. Cherevko, S. Thiele, IrO<sub>2</sub> coated TiO<sub>2</sub> core-shell microparticles advance performance of low loading proton exchange membrane water electrolyzers, *Appl. Catal. B.* 269 (2020), 118762.
- [7] S. Higashi, A. Beniya, Ultralight conductive IrO<sub>2</sub> nanostructured textile enables highly efficient hydrogen and oxygen evolution reaction: Importance of catalyst layer sheet resistance, *Appl. Catal. B.* 321 (2023), 122030.
- [8] M. Blasco-Ahicart, J. Soriano-Lopez, J.J. Carbo, J.M. Poblet, J.R. Galan-Mascaro, Polyoxometalate electrocatalysts based on earth-abundant metals for efficient water oxidation in acidic media, *Nat. Chem.* 10 (2018) 24–30.
- [9] L. He, N. Wang, B. Sun, L. Zhong, M. Yao, W. Hu, S. Komarneni, High-entropy FeCoNiMn (oxy)hydroxide as high-performance electrocatalyst for OER and boosting clean carrier production under quasi-industrial condition, *J. Clean. Prod.* 356 (2022), 131680.
- [10] R. Jia, D. Yang, D. Xu, T. Gu, Anaerobic corrosion of 304 stainless steel caused by the pseudomonas aeruginosa biofilm, *Front. Microbiol.* 8 (2017) 2335.
- [11] M.Q. Yao, J.Y. Ge, B.L. Sun, J. Hu, S.W. Koh, Y.X. Zhao, J.P. Fei, Z.X. Sun, W. Hong, Z. Chen, W.C. Hu, H. Li, Solar-driven hydrogen generation coupled with urea electrolysis by an oxygen vacancy-rich catalyst, *Chem. Eng. J.* 414 (2021), 128753.
- [12] M. Yao, H. Hu, N. Wang, W. Hu, S. Komarneni, Quaternary (Fe/Ni)(P/S) mesoporous nanorods templated on stainless steel mesh lead to stable oxygen evolution reaction for over two months, *J. Colloid Interface Sci.* 561 (2020) 576–584.
- [13] G. Hai, H. Wang, Theoretical studies of metal-organic frameworks: calculation methods and applications in catalysis, gas separation, and energy storage, *Coord. Chem. Rev.* 469 (2022) 214670.
- [14] E. Linnane, S. Haddad, F. Melle, Z. Mei, D. Fairén-Jiménez, The uptake of metal-organic frameworks: a journey into the cell, *Chem. Soc. Rev.* 51 (2022) 6065–6086.
- [15] S. Cho, C. Park, M. Jeon, J. Hwa Lee, O. Kwon, S. Seong, J. Kim, I.-D. Kim, H. Ri Moon, Interface-sensitized chemiresistor: integrated conductive and porous Metal-organic frameworks, *Chem. Eng. J.* 449 (2022), 137780.
- [16] L. Chai, Z. Hu, X. Wang, L. Zhang, T.-T. Li, Y. Hu, J. Pan, J. Qian, S. Huang, Fe<sub>7</sub>C<sub>3</sub> nanoparticles with in situ grown CNT on nitrogen doped hollow carbon cube with greatly enhanced conductivity and ORR performance for alkaline fuel cell, *Carbon* 174 (2021) 531–539.
- [17] D. Chen, Q. Sun, C. Han, Y. Guo, Q. Huang, W.A. Goddard, J. Qian, Enhanced oxygen evolution catalyzed by in situ formed Fe-doped Ni oxyhydroxides in carbon nanotubes, *J. Mater. Chem. A* 10 (2022) 16007–16015.
- [18] C. Zhou, X. Chen, S. Liu, Y. Han, H. Meng, Q. Jiang, S. Zhao, F. Wei, J. Sun, T. Tan, R. Zhang, Superdurable bifunctional oxygen electrocatalyst for high-performance zinc-air batteries, *J. Am. Chem. Soc.* 144 (2022) 2694–2704.
- [19] W. Xiang, N. Yang, X. Li, J. Linnemann, U. Hagemann, O. Ruediger, M. Heidelmann, T. Falk, M. Aramini, S. DeBeer, M. Muhler, K. Tschulik, T. Li, 3D atomic-scale imaging of mixed Co-Fe spinel oxide nanoparticles during oxygen evolution reaction, *Nat. Commun.* 13 (2022) 179.
- [20] X. Wang, A. Dong, Y. Hu, J. Qian, S. Huang, A review of recent work on using metal-organic frameworks to grow carbon nanotubes, *Chem. Commun.* 56 (2020) 10809.
- [21] G. Zhang, J. Zeng, J. Yin, C. Zuo, P. Wen, H. Chen, Y. Qiu, Iron-facilitated surface reconstruction to in-situ generate nickel–iron oxyhydroxide on self-supported FeNi alloy fiber paper for efficient oxygen evolution reaction, *Appl. Catal. B.* 286 (2021), 119902.
- [22] X.J. Bai, X.Y. Lu, R. Ju, H. Chen, L. Shao, X. Zhai, Y.N. Li, F.Q. Fan, Y. Fu, W. Qi, Preparation of MOF film/aerogel composite catalysts via substrate-seeding secondary-growth for the oxygen evolution reaction and CO<sub>2</sub> cycloaddition, *Angew. Chem. Int. Ed.* 60 (2021) 701–705.
- [23] S. Halis, N. Reimer, A. Klinkebiel, U. Lüning, N. Stock, Four new Al-based microporous metal-organic framework compounds with MIL-53-type structure containing functionalized extended linker molecules, *Micropor. Mesopor. Mater.* 216 (2015) 13–19.
- [24] P. Nachtigall, C.O. Arean, Themed issue on characterization of adsorbed species, *Phys. Chem. Chem. Phys.* 12 (2010) 6307–6308.
- [25] C. Schlusener, D.N. Jordan, M. Xhinovci, T.J. Matemb Ma Ntep, A. Schmitz, B. Giesen, C. Janiak, Probing the limits of linker substitution in aluminum MOFs through water vapor sorption studies: mixed-MOFs instead of mixed-linker CAU-23 and MIL-160 materials, *Dalton Trans.* 49 (2020) 7373–7383.
- [26] W. Chen, Q. Xin, G. Sun, S. Yang, Z. Zhou, Q. Mao, P. Sun, Effects of dissolved iron and chromium on the performance of direct methanol fuel cell, *Electrochim. Acta* 52 (2007) 7115–7120.
- [27] J. Yu, J. Cao, Z. Yang, W. Xiong, Z. Xu, P. Song, M. Jia, S. Sun, Y. Zhang, J. Zhu, One-step synthesis of Mn-doped MIL-53(Fe) for synergistically enhanced generation of sulfate radicals towards tetracycline degradation, *J. Colloid Interface Sci.* 580 (2020) 470–479.
- [28] D. Salionov, O.O. Semivrazhskaya, N.P.M. Casati, M. Ranocchiari, S. Bjelic, R. Verel, J.A. van Bokhoven, V.L. Sushkevich, Unraveling the molecular mechanism of MIL-53(Al) crystallization, *Nat. Commun.* 13 (2022) 3762.
- [29] D. Jiang, Y. Zhu, M. Chen, B. Huang, G. Zeng, D. Huang, B. Song, L. Qin, H. Wang, W. Wei, Modified crystal structure and improved photocatalytic activity of MIL-53 via inorganic acid modulator, *Appl. Catal. B.* 255 (2019), 117746.
- [30] B. Yuan, C. Li, L. Guan, K. Li, Y. Lin, Prussian blue analog nanocubes tuning synthesis of coral-like Ni<sub>3</sub>S<sub>2</sub>@MIL-53(NiFeCo) core-shell nanowires array and boosting oxygen evolution reaction, *J. Power Sources* 451 (2020), 227295.
- [31] J. Benecke, S. Mangelsen, T.A. Engesser, T. Weyrich, J. Junge, N. Stock, H. Reinsch, A porous and redox active ferrocenedicarboxylic acid based aluminium MOF with a MIL-53 architecture, *Dalton Trans.* 48 (2019) 16737–16743.
- [32] M. Xie, Y. Ma, D. Lin, C. Xu, F. Xie, W. Zeng, Bimetal-organic framework MIL-53 (Co-Fe): an efficient and robust electrocatalyst for the oxygen evolution reaction, *Nanoscale* 12 (2020) 67–71.
- [33] T.A. Vu, G.H. Le, C.D. Dao, L.Q. Dang, K.T. Nguyen, Q.K. Nguyen, P.T. Dang, H.T. K. Tran, Q.T. Duong, T.V. Nguyen, G.D. Lee, Arsenic removal from aqueous solutions by adsorption using novel MIL-53(Fe) as a highly efficient adsorbent, *RSC Adv.* 5 (2015) 5261–5268.
- [34] Y. Ma, J. Huang, L. Lin, Q. Xie, M. Yan, B. Qu, L. Wang, L. Mai, D.-L. Peng, Self-assembly synthesis of 3D graphene-encapsulated hierarchical Fe<sub>3</sub>O<sub>4</sub> nano-flower architecture with high lithium storage capacity and excellent rate capability, *J. Power Sources* 365 (2017) 98–108.
- [35] A. Kai, Y. Terayama, K. Ogawa, T. Shoji, Characterization of oxide film formed on austenitic stainless steel by in situ micro Raman spectroscopy, *Key Eng. Mater.* 297–300 (2005) 2806–2812.
- [36] M.W. Louie, A.T. Bell, An investigation of thin-film Ni-Fe oxide catalysts for the electrochemical evolution of oxygen, *J. Am. Chem. Soc.* 135 (2013) 12329–12337.
- [37] B.S. Yeo, A.T. Bell, Enhanced activity of gold-supported cobalt oxide for the electrochemical evolution of oxygen, *J. Am. Chem. Soc.* 133 (2011) 5587–5593.
- [38] S. Yuan, J. Peng, B. Cai, Z. Huang, A.T. Garcia-Esparza, D. Sokaras, Y. Zhang, L. Giordano, K. Akkiraju, Y.G. Zhu, R. Hubner, X. Zou, Y. Roman-Leshkov, Y. Shao-Horn, Tunable metal hydroxide-organic frameworks for catalysing oxygen evolution, *Nat. Mater.* 21 (2022) 673–680.
- [39] L. Zhong, J.Y. Ding, X. Wang, L.L. Chai, T.T. Li, K.Z. Su, Y. Hu, J.J. Qian, S. M. Huang, Structural and morphological conversion between two Co-based MOFs for enhanced water oxidation, *Inorg. Chem.* 59 (2020) 2701–2710.
- [40] M.P. Watts, T.V. Khijniak, C. Boothman, J.R. Lloyd, Treatment of alkaline Cr(VI)-contaminated leachate with an alkaliphilic metal-reducing bacterium, *Appl. Environ. Microbiol.* 81 (2015) 5511–5518.

- [41] Y. Wang, S. Tao, H. Lin, S. Han, W. Zhong, Y. Xie, J. Hu, S. Yang, NaBH<sub>4</sub> induces a high ratio of Ni<sup>3+</sup>/Ni<sup>2+</sup> boosting OER activity of the NiFe LDH electrocatalyst, RSC Adv. 10 (2020) 33475–33482.
- [42] C. Feng, Z. Zhang, D. Wang, Y. Kong, J. Wei, R. Wang, P. Ma, H. Li, Z. Geng, M. Zuo, J. Bao, S. Zhou, J. Zeng, Tuning the electronic and steric interaction at the atomic interface for enhanced oxygen evolution, J. Am. Chem. Soc. 144 (2022) 9271–9279.
- [43] H. Shin, H. Xiao, W.A. Goddard III, In silico discovery of new dopants for Fe-doped Ni oxyhydroxide (Ni<sub>1-x</sub>Fe<sub>x</sub>OOH) catalysts for oxygen evolution reaction, J. Am. Chem. Soc. 140 (2018) 6745–6748.